Design and Optimization of High-Performance 1.3 μm VCSELs

Joachim Piprek,* Manish Mehta, and Vijay Jayaraman

Electrical and Computer Engineering Dept., University of California, Santa Barbara, CA 93106

ABSTRACT

This paper discusses the design and the internal device physics of novel high-performance vertical-cavity surface-emitting lasers (VCSELs) emitting at 1.32 μm wavelength. Our VCSEL design features intra-cavity ring contacts, strain-compensated AlGaInAs quantum wells, and an AlInAs/InP tunnel junction. The tunnel junction is laterally confined forming an aperture for current injection and wave guiding. Undoped AlGaAs/GaAs mirrors are bonded on both sides to the InP-based active region. These devices have recently demonstrated continuous-wave (CW) lasing at stage temperatures up to 134°C, the highest temperature reported thus far for any long-wavelength VCSEL. In order to increase the single mode output power at high temperatures, we simulate, analyze, and optimize our VCSEL using advanced numerical software tools. The two-dimensional model self-consistently combines electrical, optical, thermal and gain calculations. It gives good agreement with measurements after careful calibration of material parameters. Design optimization promises single mode output power of 2mW in CW operation at 80°C ambient temperature.

Keywords: long-wavelength vertical-cavity surface-emitting laser diode, VCSEL, tunnel junction, wafer bonding, numerical simulation

1. INTRODUCTION

Long-wavelength vertical-cavity surface-emitting lasers (VCSELs) are desired low-cost light sources for applications in fiberoptic communication. In contrast to the rapid development of GaAs-based VCSELs emitting at shorter wavelengths, the performance of InP-based long-wavelength devices is severely limited by disadvantageous material properties. With the lower bandgap of the InGaAsP active region, Auger recombination enhances non-radiative losses. With lower photon energy, free-carrier and intervalence band absorption (IVBA) lead to enhanced optical losses. Native InGaAsP/InP distributed Bragg reflectors (DBRs) only allow for a small variation of the refractive index that is about half the variation possible in AlGaAs. To obtain high DBR reflectances, a large number of mirror layers has to be grown causing significant diffraction losses. InGaAsP also exhibits low thermal conductivity due to disorder scattering of phonons. Thus, thick InGaAsP/InP DBRs block the thermal flux to the stage and lead to a strong increase of the active region temperature in continuous-wave (CW) operation. Therefore, several alternative material and design concepts for 1.3 μm VCSELs have been developed, including GaAs-based and hybrid approaches.

A main challenge with long-wavelength VCSELs is the *simultaneous* demonstration of high-temperature, high-speed, and high-power fundamental mode lasing. In order to achieve this goal, several design trade-offs need to be balanced carefully. For instance, large current apertures and thick InP cavity layers are advantageous for high-power and high-temperature operation, respectively. However, single mode lasing requires small apertures and high-speed modulation requires thin vertical cavities. Finding the optimum design by experimental methods is expensive and time-consuming. We here employ physics-based self-consistent VCSEL simulation software in order to analyze and optimize the internal device physics.[1] Carrier transport is simulated using a finite-element drift-diffusion model. The heat flux equation is included to address self-heating effects. Gain calculations are based on 4x4 kp bandstructure computations for the strained quantum wells. The transmission matrix method is employed for optical simulation in order to obtain the vertical optical intensity profile. The lateral optical modes are given by Bessel functions which are adjusted to measured VCSEL near fields. Further details of the model can be found elsewhere.[2] Material parameters are carefully calibrated in the simulation in order to achieve good agreement with the measurements.

* Corresponding author, e-mail: piprek@ieee.org

Physics and Simulation of Optoelectronic Devices XII, edited by Marek Osinski,
Hiroshi Amano, Fritz Henneberger, Proceedings of SPIE Vol. 5349 (SPIE,
Bellingham, WA, 2004) · 0277-786X/04/$15 · doi: 10.1117/12.543062

2. VCSEL DESIGN

Our device design follows the hybrid approach by joining highly reflective GaAs-based mirrors and high-gain InP-based active layers in InP/GaAs wafer bonded VCSELs (Fig. 1, Tab. 1). Compared to our previous design of wafer-bonded 1.55 μm VCSELs [3], this design of 1.3 μm VCSELs includes three main new features:

(1) Strained AlGaInAs quantum wells (QWs) offering a larger conduction band offset than InGaAsP QWs which is essential to reduce electron leakage at high temperatures.

(2) Intra-cavity contacts feed the current directly into highly conductive n-InP layers, without passing wafer-bonded interfaces, thereby reducing reliability risks.

(3) A buried tunnel junction is located above the MQW region (Fig. 2). This junction has multiple advantages in our VCSEL, it reduces the intervalence-band absorption related to p-doping, it allows for lower threshold bias due to higher carrier mobility in n-InP, and it provides lateral electrical and optical confinement by selective etching.

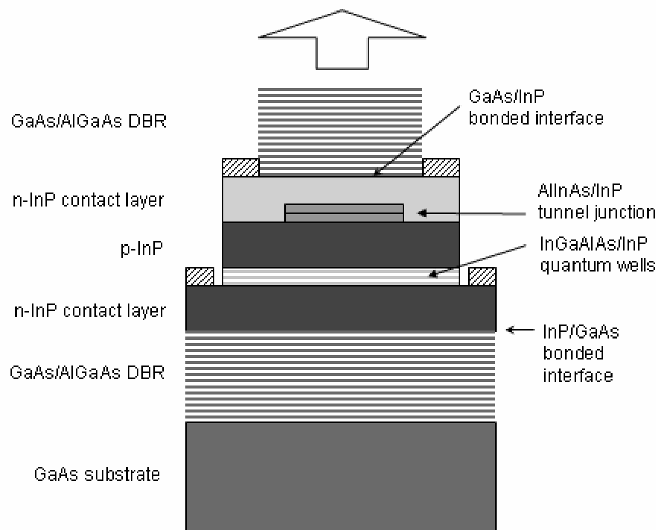

Fig. 1: Schematic structure of our vertical cavity laser.

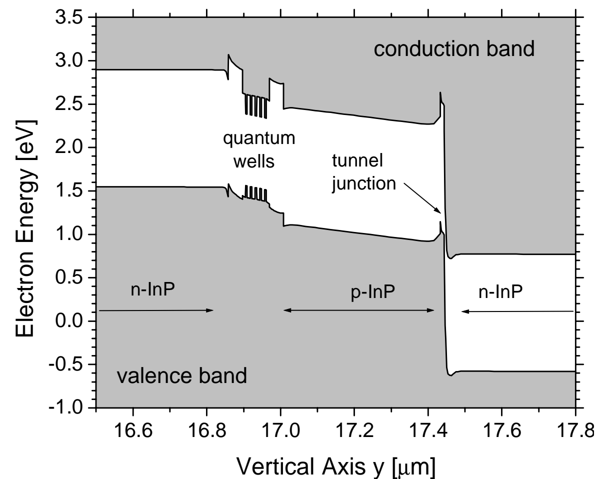

Fig. 2: Energy band diagram of the InP-based active region.

We have studied different design approaches for the lateral confinement. Our first device generation combined a tunnel junction with the commonly used lateral oxidation layer within the top DBR.[4] However, the performance was mainly limited by lateral current leakage due to the high carrier (electron) mobility between aperture and tunnel junction. We therefore explored the lateral under etching of the MQW active region which promises better current confinement.[5] The performance of this second device generation was poor due to misalignment of etched aperture and top DBR pillar. The third alternative investigated was patterned wafer bonding onto disk-shaped etched tunnel junctions.[6] This approach allows for precise control of the aperture size which is not possible with lateral oxidation or etching. In order to accommodate intra-cavity contacts, our final design covers the etched tunnel junction by a re-grown n-InP contact layer before wafer bonding (Fig. 1).[7] The etched tunnel junction introduces a step of about 30 nm in the top surface of the re-grown contact layer. This surface is sufficiently planar to permit wafer bonding of the top AlGaAs/GaAs mirror.

3. EXPERIMENTAL RESULTS

We here discuss experimental results for three VCSELs with different tunnel junction aperture size and different gain-mode offset.[8,9] This offset is illustrated in Fig. 3 and it is a crucial VCSEL design parameter in order to achieve high-temperature operation. With increasing temperature, the gain spectrum moves to longer wavelength at a faster rate than

the wavelength of the lasing mode. With negative gain-mode offset, as shown in Fig. 3, the modal gain increases with higher temperature. Larger gain – mode offset allows for lasing at higher temperatures. However, larger offset also reduces the available gain at room temperature and the maximum output power. Thus, careful tuning of the gain – mode offset is required for optimum performance (see Sec. 5).

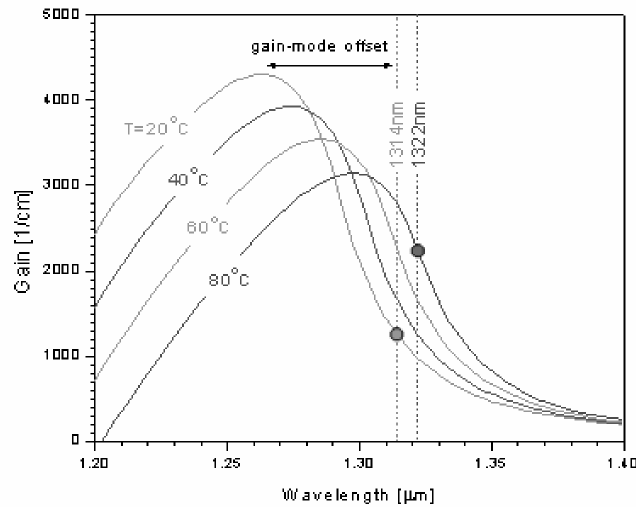

Fig. 3 Calculated gain spectra at different MQW temperatures (constant carrier density). The dashed vertical lines give the VCSEL emission wavelength at 20°C and 80°C, respectively, and the dots indicate the actual gain of the lasing mode.

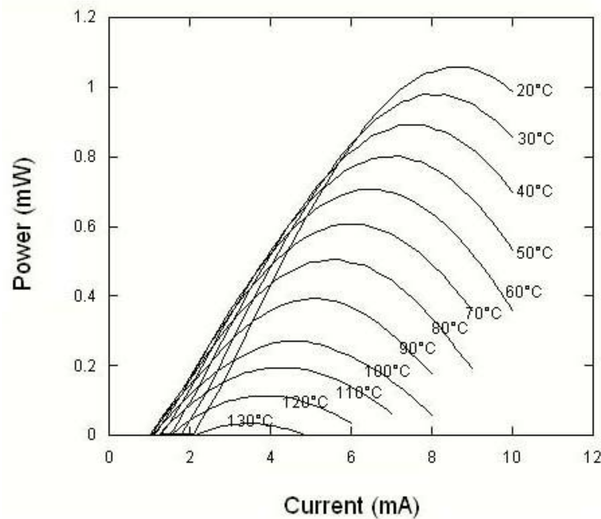

Fig. 4: Measured light-current characteristics in continuous-wave (CW) operation at different stage temperatures (8µm aperture, 66 nm offset).

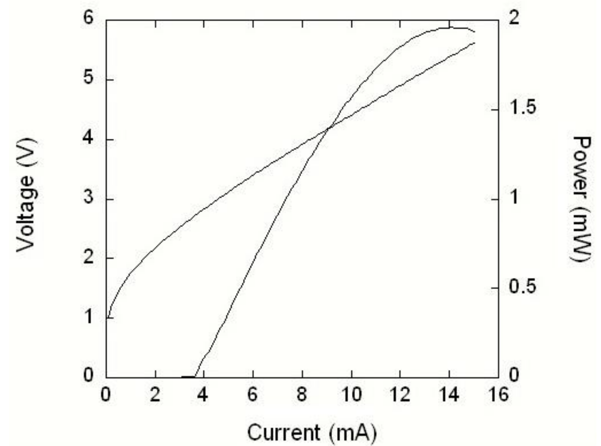

Fig. 5: CW light-current and current-voltage characteristics measured at room temperature (12 µm aperture, 51 nm offset).

All devices in this section employ 5 quantum wells, 25 top DBR periods and 31 bottom DBR periods. The exact position of the gain peak wavelength is unknown, however, it is close to the peak of the measured photoluminescence (PL) spectrum, which is used in the following to determine an offset parameter. Figure 4 gives light-current (LI) characteristics for 66 nm PL – mode offset and 8 micron aperture. This large offset results in lasing up to a maximum stage temperature of 134°C, the highest temperature ever achieved with any long-wavelength VCSEL. For this device, the maximum output power at room temperature is slightly above 1 mW.

Figure 5 gives the LI and current-voltage curve for a VCSEL with 12 micron aperture and with 51 nm PL - mode offset. Due to the larger spot size and the smaller offset, an enhanced differential efficiency of 30% and a larger output power of almost 2mW is achieved at room temperature. The threshold voltage of 2.7 V and the differential resistance of 245 Ω are relatively high. The maximum CW operating temperature of this device is 100°C. The larger aperture leads to multimode operation at higher temperatures. 66°C fundamental mode operation with almost 1 mW output power is observed with our third VCSEL that combines an 8 micron aperture with 51 nm PL – mode offset (Fig. 6). This device operates up to 123°C stage temperature.

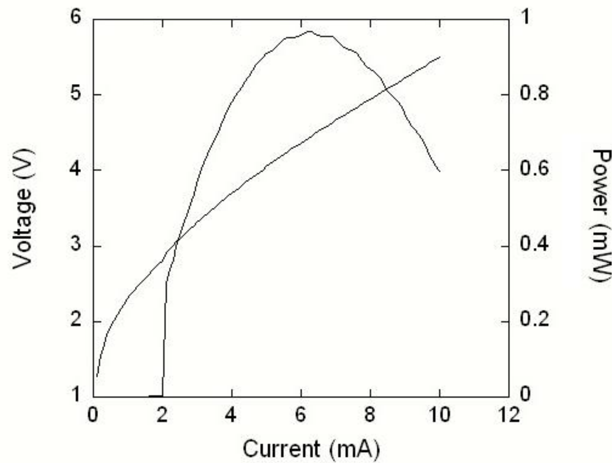

Fig. 6a: CW light-current and current-voltage characteristics measured at 66°C (8 μm aperture, 51 nm offset).

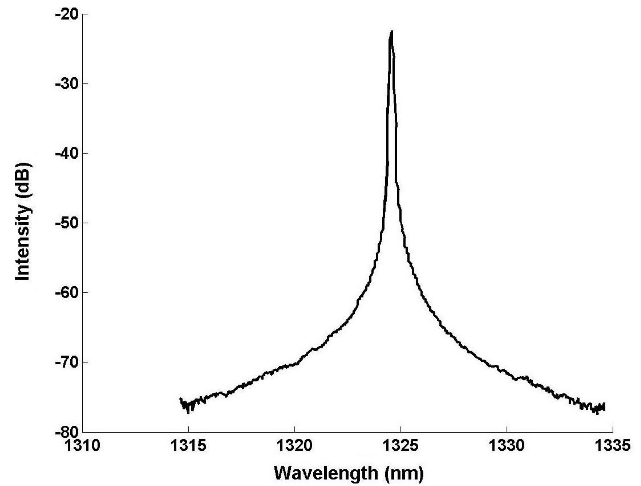

Fig. 6b: Modal spectrum at 66°C (8 μm aperture, 51 nm offset).

4. SIMULATION AND ANALYSIS

In this section, we use advanced numerical simulation software[1] in order to analyze the internal physics and the performance limits of our VCSELs. The device model combines electrical, optical, thermal, and gain calculations self-consistently.[2] Such complex models include a large number of material parameters which need to be calibrated carefully for realistic simulation results. Table 1 lists key parameters for all the epitaxial layers of our VCSEL. The parameter calibration process is described in the following and it leads to good agreement between simulations and measurements as shown in Figs. 7 and 8. All measurements are for the same VCSEL with 8 μm aperture. Nearfield measurements show a weak optical confinement with a fundamental mode diameter of about 13 μm which is adopted in the following.

The peak of the calculated spontaneous emission spectrum coincides with the measured PL peak (Fig. 7) when quantum well bandgap renormalization is considered with

$$\Delta E_g = \xi \left(\frac{n+p}{2} \right)^{1/3} \tag{1}$$

and $\xi = -10^{-10}$ eV/m (n and p are respectively the densities of electrons and holes). Using a Lorentz broadening function with 50 fs scattering time gives good agreement with the important long-wavelength side of the spectrum (cf. Fig. 3). The short-wavelength side is not matched very well, i.e., LI simulation beyond the power roll-off is less reliable (cf. Fig. 8). The measured PL peak shifts at a rate of 0.45 nm/K with increasing temperature. This translates into a thermal bandgap shift of 0.334 meV/K, which is adopted for all layers in the simulation.

Parameter	d	N	μ	n	α	κ
Unit	μm	cm^{-3}	cm^2/ Vs		cm^{-1}	W/ cm K
i-$Al_{0.92}Ga_{0.08}As$ (DBR, 27x)	0.111	nid	-	2.946	0.0	0.22
i-GaAs (DBR, 27x)	0.096	nid	-	3.411	0.0	0.22
n-InP (spacer, contact)	0.388	$5\ 10^{17}$	2600	3.22	1.0	0.68
n-InP (tunnel junction)	0.020	$1.5\ 10^{19}$	1100	3.22	30	0.68
p-$In_{0.52}Al_{0.48}As$ (tun. junct.)	0.010	$1.5\ 10^{20}$	10	3.24	1950	0.05
p-InP (spacer)	0.4325	$2\ 10^{17}$	100	3.22	2.6	0.68
i-$In_{0.52}Al_{0.48}As$ (stopper)	0.0382	nid	p:50	3.24	0.0	0.05
$In_{0.68}Ga_{0.175}Al_{0.145}As$ (QW)	0.0044	nid	50	3.49	α(n,p)	0.05
$In_{0.44}Ga_{0.326}Al_{0.234}As$ (bar.)	0.0084	nid	50	3.49	α(n,p)	0.05
i-$In_{0.52}Al_{0.48}As$ (stopper)	0.0382	nid	n:4800	3.24	0.0	0.05
n-InP (spacer, contact)	0.4325	$1.2\ 10^{18}$	2100	3.22	2.4	0.68
i-GaAs (DBR, 31x)	0.096	nid	-	3.411	0.0	0.22
i-$Al_{0.92}Ga_{0.08}As$ (DBR, 31x)	0.111	nid	-	2.946	0.0	0.22
i-GaAs (substrate)	300	nid	-	3.411	0.0	0.44

Tab. 1: Epitaxial layer structure with key parameters at room temperature (d- thickness, N – doping, μ - majority carrier mobility, α - absorption, κ – thermal conductivity, nid – not intentionally doped, α(n,p) – see Eq. 2).

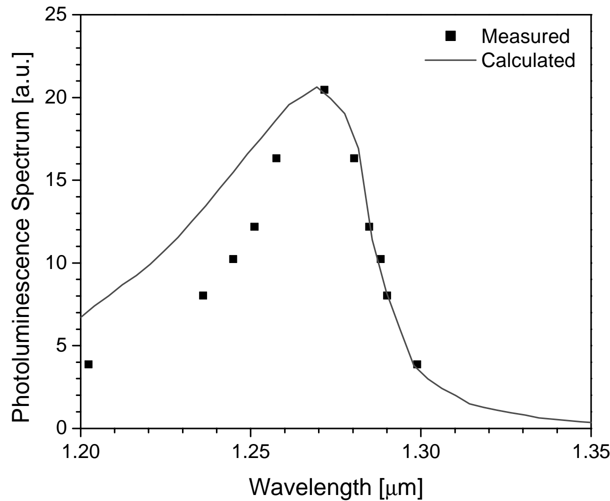

Fig. 7: Comparison of measured and simulated PL spectrum at room temperature.

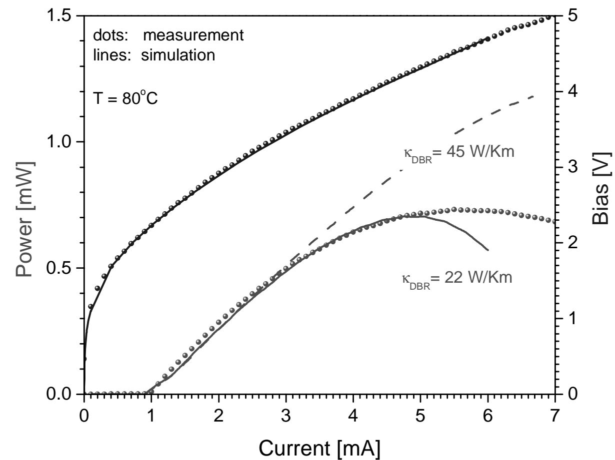

Fig. 8: Comparison of measured and simulated IV and LI characteristics at elevated temperature.

It is essential for the optical simulation of the laser diode to use accurate refractive index values for each material. The popular Sellmeier formulas for the refractive index [10] are often inaccurate for photon energies near the band gap. Instead, we employ the Adachi model which was developed for energies close to the bandgap (Tab. 1).[11] The thermal change of the refractive index is assumed 2×10^{-4}/K for InP-based layers and 3×10^{-4}/K for GaAs-based layers,[12] which results in good agreement with the measured shift of the emission wavelength. Internal optical loss in 1.3 μm lasers is affected by free carriers (n,p) as well as by photon scattering (α_s) according to

$$\alpha(n,p) = \alpha_s + k_n\, n + k_p\, p. \qquad (2)$$

It is expected to be mainly dominated by intervalenceband absorption ($k_p = 13 \times 10^{-22}$ m^2) [13] and less by free electrons ($k_n = 2 \times 10^{-22}$ m^2). The scattering loss parameter is fitted to $\alpha_s = 3$ /cm using the measured LI characteristic.

The drift-diffusion model of carrier transport considers Fermi statistics and thermionic emission at hetero-barriers. Thermionic emission is mainly controlled by the offset of conduction band (ΔE_c) and valence band (ΔE_v). For the AlGaInAs material system, a band offset ratio of $\Delta E_c/\Delta E_g = 0.72$ is commonly assumed. At the type-II interface of AlInAs and InP, we assume ΔE_c =292 meV and ΔE_v = 147 meV (cf. Fig. 2). The Auger recombination rate is given by $(C_n n+C_p p)(np-n_i^2)$ with the intrinsic carrier density n_i. Both the Auger coefficients are represented by a temperature dependent function

$$C(T) = C_0(T_0) \times \exp\left[\frac{E_A}{k}\left(\frac{1}{T_0} - \frac{1}{T}\right)\right] \qquad (3)$$

with the Boltzmann constant k. The LI fit results in $C_0 = 1.15 \times 10^{-29} cm^6s^{-1}$ at T_0 = 298 K and E_A = 160 meV. This value of C_0 is in the middle of the range reported in the literature.[2] E_A is slightly larger than in previous investigations of 1.3 μm InGaAsP/InP lasers.[14] The other quantum well recombination mechanisms are less important. The spontaneous recombination rate is obtained from the integration of the emission spectrum. The defect recombination lifetime is assumed as 10 ns within the quantum well and 100 ns elsewhere. The carrier mobility is a sophisticated function of composition, doping, local electric field, and temperature. Analytical functions are derived for binary materials.[2] Thus, some uncertainty remains with the mobilities in Tab. 1, especially for ternary and quaternary semiconductors. We here only adjust the hole mobility of the p-InP spacer layer which is considered the bottleneck for the carrier transport in our device. A value of 70 cm^2/Vs gives good agreement with the IV characteristic measured at 80°C (Fig. 8).

This adjustment is especially important for CW simulations because the mobility also affects the Joule heat generated inside the device. Good agreement with the measured IV curve is a prerequisite to correctly simulate the generated heat power which affects the measured LI curve and causes the typical power roll-off at higher current (Fig. 8). The last remaining fit parameter is the thermal conductivity of the DBR. This number is affected by phonon scattering at the DBR interfaces and it cannot be deduced from bulk thermal conductivity data. [15] A value of κ_{DBR} = 22 W/mK gives the best agreement with the measured power roll-off. For comparison, the simulated LI curve with κ_{DBR} = 45 W/mK is also shown in Fig. 8.

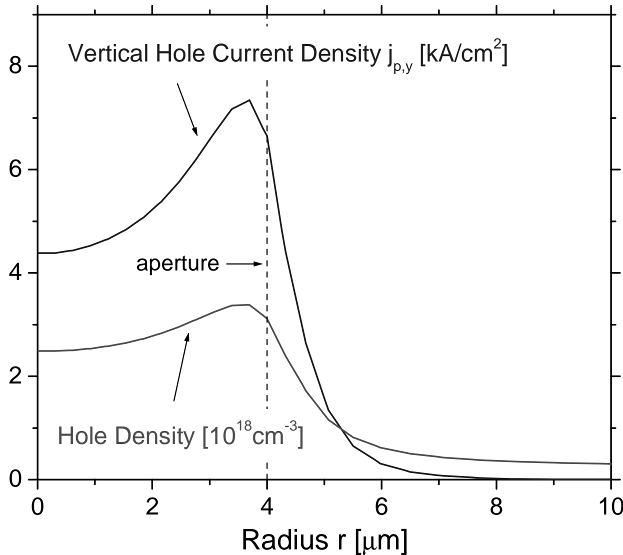

Fig. 9: Lateral profile of hole injection current density and hole density within the top quantum well (I = 5 mA).

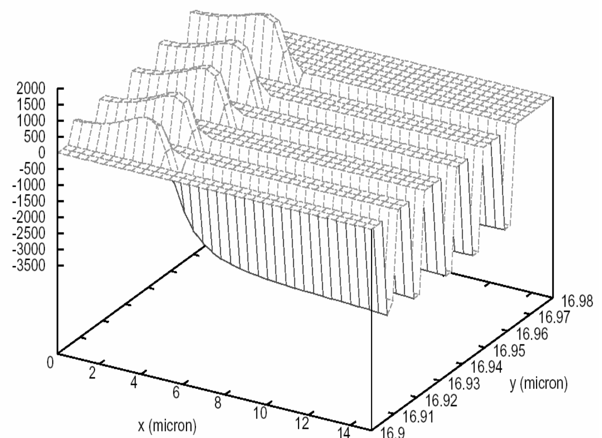

Fig. 10: 2D Surface plot of the optical gain within the MQW region (I = 5 mA).

Based on this good agreement with measurements, we can now use the simulation to quantitatively analyze performance limitations of our VCSEL. First, we investigate the lateral quantum well carrier confinement as imposed by the tunnel junction aperture of 8 µm diameter. Figure 9 confirms relatively weak lateral current spreading in the p-InP layer leading to a good lateral carrier confinement within the quantum wells. The lateral gain profile is shown in Fig. 10 as surface plot for all five quantum wells. According to the carrier density minimum in the center of the device, the gain profile also exhibits a minimum in the center. Maximum gain occurs near the aperture where it potentially supports higher order transversal modes. Thus, the uniformity of the current injection through the tunnel junction aperture needs to be improved in order to better support the fundamental mode which has an intensity maximum in the center.

Figure 11 gives a 2D vector plot of the hole current indicating hole leakage from the MQW region into the n-doped InP spacer, where the holes recombine with electrons. This leakage is supported by the n-side AlInAs cladding layer underneath the MQW, which provides little hole confinement (cf. Fig. 2). In order to improve the VCSEL performance, this AlInAs layer should be removed since the InP layer gives a larger valence band offset.

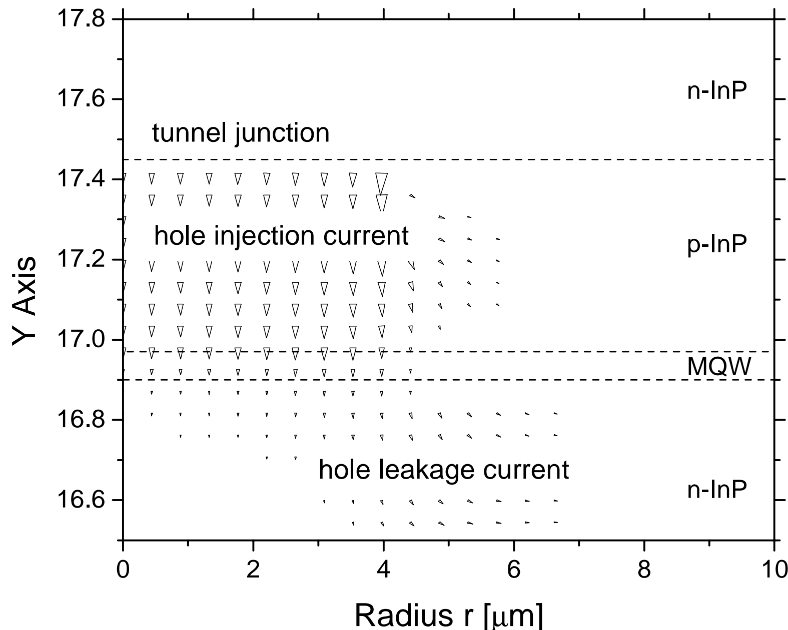

Fig. 11: 2D vector plot of the hole current density indicating hole leakage from the MQW region.

5. DESIGN OPTIMIZATION

1.3 µm VCSEL applications in telecommunication systems require single fundamental mode operation with more than 1 mW output power at 80°C ambient temperature. These performance goals need to be achieved simultaneously with the same device design. In the following, we optimize our device design using the insight gained in the previous section. A first step is the reduction of hole leakage by removing the lower AlInAs layer (Fig. 12). As a result, the hole leakage into the n-InP spacer layer is reduced by two orders of magnitude (Fig. 13). This restriction of carrier loss significantly enhances the internal quantum efficiency of the laser which leads to a larger slope efficiency as shown in Fig. 14. The internal bias is slightly lower which results in less self-heating.

Figure 15 shows the benefits of higher n-doping. The resistance of the top n-InP layer is reduced which results in less heating and more uniform current distribution within the aperture. However, the impact on the LI curve is relatively small. Much larger effect has an increased n-doping of the tunnel junction which reduces the junction bias by almost 1 V and gives a significant output power enhancement (solid curves).

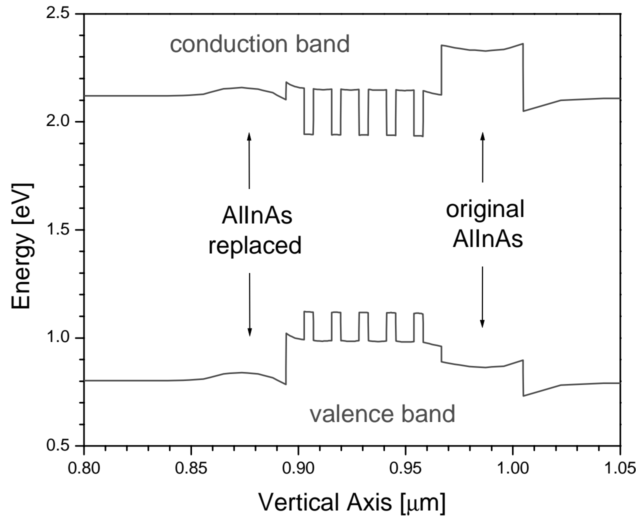

Fig. 12: Energy band diagram for device design without lower AlInAs layer.

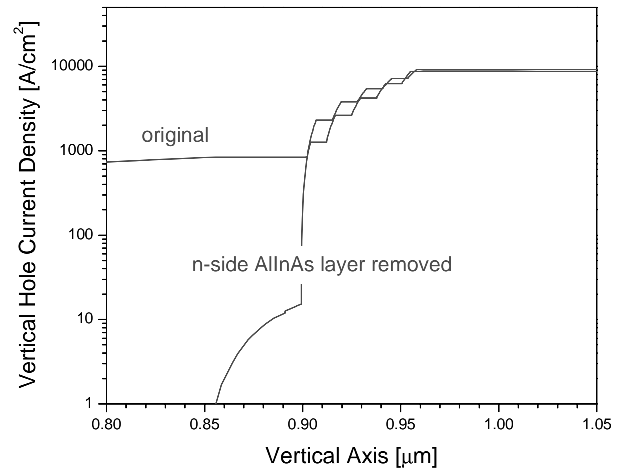

Fig. 13: Vertical hole current profile for device design without lower AlInAs layer.

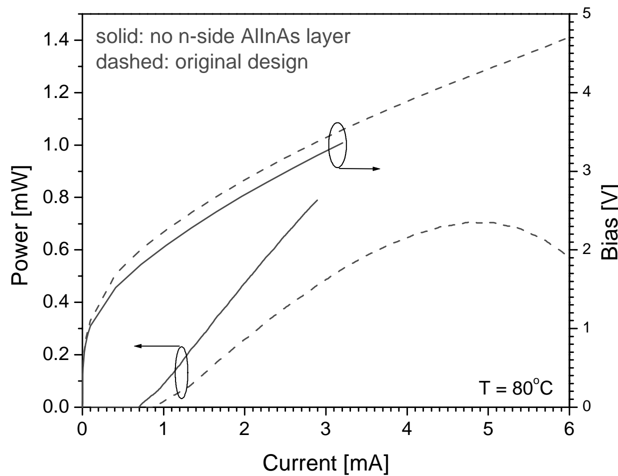

Fig. 14: Simulated LIV curves before (dashed) and after (solid) removal of the lower AlInAs layer (the solid line ends at about 3 mA since the simulation crashed at this point).

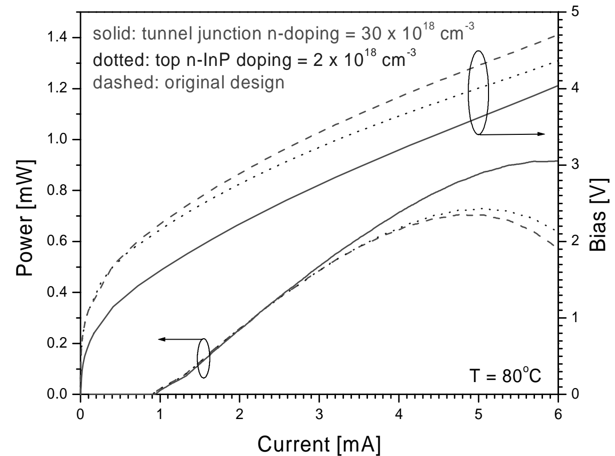

Fig. 15: Simulated LIV curves for increased n-doping of the top InP layer (dotted) and the tunnel junction (solid). The original design is represented by the dashed curves.

In order to reduce the bias and the intervalence band absorption, a thinner p-InP spacer layer above the MQW seems advantageous. We here simulate a reduction by half of the internal wavelength from 432.5 nm to 227.5 nm thickness. The resulting LIV curves are somewhat surprising (Fig. 16) as the bias is unchanged and the maximum output power is smaller than with the original design. An explanation can be derived from Fig. 17 which shows the lateral gain profile for both cases as well as compared to the fundamental mode profile. Obviously, the thinner p-InP restricts the lateral current spreading which gives the same overall bias and which reduces the area of positive gain. As a consequence, the

fundamental mode experiences stronger absorption in its tail regions which reduces the modal gain as well as the maximum output power.

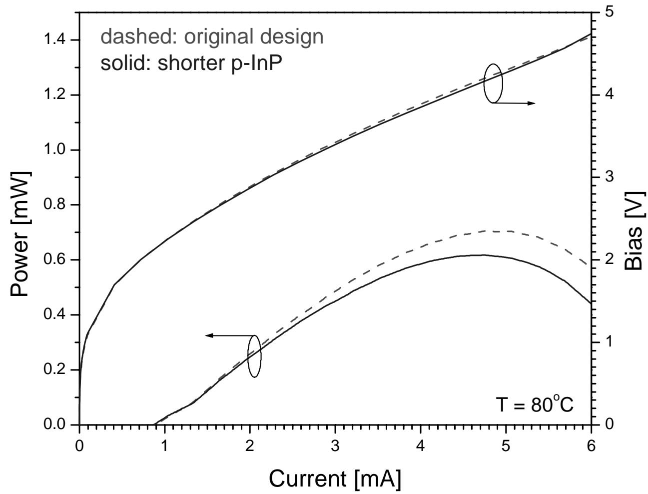

Fig. 16: Simulated LIV curves with shorter p-InP layer (solid) compared to the original (dashed).

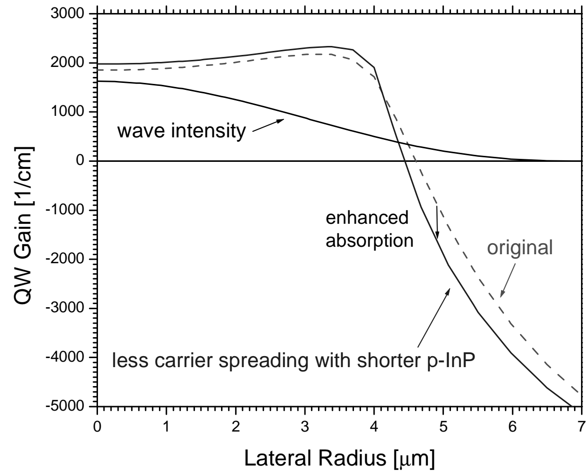

Fig. 17: Lateral gain profile within the top quantum well for the original design (dashed) and with thinner p-InP layer (solid). The intensity of the fundamental mode is plotted in the upper part.

Further design studies in search for a maximum output power lead to an optimized gain – mode offset of 32 nm, an optimized number of 28 top DBR periods, and a larger aperture of 10 μm. The original number of 5 quantum wells turns out to be optimum. Including the changes discussed above (except the thinner p-InP), the LIV characteristics for this optimized VCSEL design are shown in Fig. 18 with 0.6 mA threshold current, 1 V threshold bias, and a maximum fundamental mode power close to 2 mW.

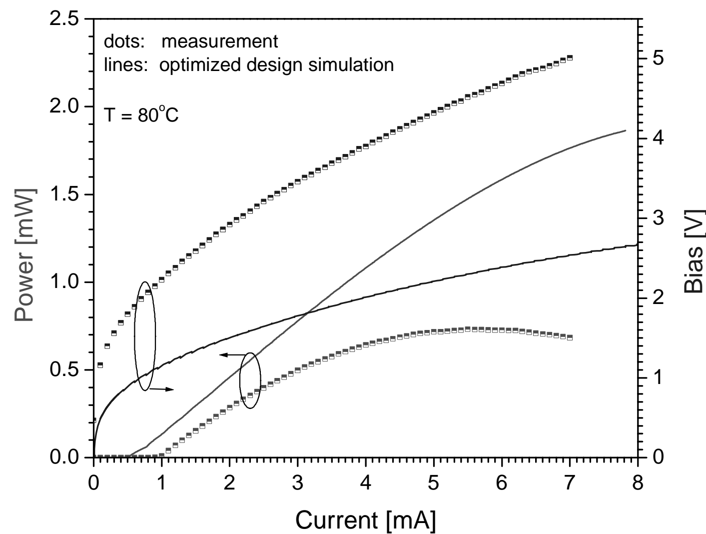

Fig. 18: Simulated LIV curves (lines) for the optimized VCSEL design compared to measurements on the original VCSEL (dots).

6. CONCLUSION

We have demonstrated by advanced numerical simulation that design optimization of our VCSEL can lead to simultaneous demonstration of high-temperature and high-power single mode lasing with the same device.

ACKNOWLEDGEMENT

This research was supported by Walsin USA, Sun Microsystems, and by an University of California Discovery grant (UC-SMART).

REFERENCES

[1] PICS3D by Crosslight Software, 2003.

[2] J. Piprek, *Semiconductor Optoelectronic Devices – Introduction to Physics and Simulation*, Academic Press, San Diego, 2003.

[3] A. Karim, J. Piprek, P. Abraham, D. Lofgreen, Yi-Jen Chiu, and J. E. Bowers, "1.55 µm Vertical-Cavity Laser Arrays for Wavelength-Division Multiplexing", IEEE J. Sel. Topics Quantum Electron., Vol. 7, pp. 178-183, 2001.

[4] J. Piprek, R. Glew, and Yi-Jen Chiu, "Wafer-Bonded 1.3-micron Vertical Cavity Laser", IEEE Semiconductor Laser Workshop, Long Beach, CA, 2002.

[5] J. Piprek , A. Bregy, Y-J. Chiu, V. Jayaraman, and J. E. Bowers; "Lateral-Cavity Design for Long-Wavelength Vertical-Cavity Lasers," Proc. NanoTech Conf., San Francisco, 2003.

[6] J. Piprek, "Advanced Analysis of Vertical Cavity Lasers" , Proc. Int. Conf. Mixed Design MIXDES, Lodz, Poland, 2003.

[7] V. Jayaraman, M. Mehta, A. W. Jackson, S. Wu, Y. Okuno, J. Piprek, and J.E. Bowers, " High power 1320 nm Wafer-Bonded VCSELs with Tunnel Junctions, " IEEE Photonics Technology Letters, Vol. 15, No. 11, pp. 1495-1497, 2003.

[8] M. Mehta, V. Jayaraman, A. Jackson, Y. Okuno, S. Wu, J. Piprek, and J. Bowers, "134°C continuous-wave operation of a 1.33 µm wafer-bonded VCSEL," CLEO Postdeadline Paper CThPDC10, Baltimore, June 2003.

[9] Manish Mehta, Vijay Jayaraman, Andrew Jackson, Shaomin Wu, Yae Okuno, Joachim Piprek, and John E. Bowers, "Wafer-bonded Vertical-Cavity Lasers with Tunnel Junction," SPIE-ITCom Symp. *Semiconductor Optoelectronic Devices for Lightwave Communication*, Orlando, SPIE Proc. 5248-20, 2003.

[10] M. J. Mondry, D. I. Babic, J. E. Bowers, L.A. Coldren, "Refractive indexes of (Al,Ga,In)As epilayers on InP for optoelectronic applications," IEEE Photonics Technology Letters, vol. 4, no. 6, pp.627-630, 1992.

[11] S. Adachi, *Physical Properties of III-V Semiconductor Compounds*, Wiley, New York, 1992.

[12] J. Piprek, D. I. Babic, and J. E. Bowers, "Simulation and analysis of 1.55-micron double-fused vertical-cavity lasers," Journal of Applied Physics, vol. 81, pp. 3382-3390, 1997.

[13] C. H. Henry, R. A. Logan, F. R. Merritt, and J. P. Luongo, "The effect of intervalence band absorption on the thermal behavior of InGaAsP lasers," IEEE J. Quantum Electron., vol. 19, pp. 947-952, 1983.

[14] S. Mogg and J. Piprek, "Optimization of the barrier height in 1.3-micron InGaAsP multiple-quantum-well active regions for high temperature operation," in: *Physics and Simulation of Optoelectronic Devices IX*, SPIE Proc. 4283-29, 2001.

[15] J. Piprek, T. Troger, B. Schroter, J. Kolodzey, and C. S. Ih, "Thermal conductivity reduction in GaAs-AlAs distributed Bragg reßectors," IEEE Photonics Technology Letters, vol. 10, no. 1, pp. 81-83, 1998.